# Characterization of the seismic response of gas-hydrate bearing sediments

**Juan E. Santos[1,2,3], Patricia M. Gauzellino[4], José M. Carcione[5], and Jing Ba[1]**

[1]School of Earth Sciences and Engineering, Hohai University, Nanjing, 211100, China

[2]Universidad de Buenos Aires, Facultad de Ingeniería, Instituto del Gas y del Petróleo, Av. Las Heras 2214 Piso 3, C1127AAR Buenos Aires, Argentina

[3]Department of Mathematics, Purdue University, 150 N. University Street, West Lafayette, Indiana, 47907-2067, USA

[4]Departamento de Geofísica Aplicada, Facultad de Ciencias Astronómicas y Geofísicas, Universidad Nacional de La Plata, Paseo del Bosque s/n, La Plata, B1900FWA, Argentina

[5]Istituto Nazionale di Oceanografia e di Geofisica Sperimentale (OGS), Borgo Grotta Gigante 42c, 34010 Sgonico, Trieste, Italy

**Key Points:**

- Sediments contained gas-hydrates are modeled as composite materials consisting of the rock frame, ice and water.
- Effective viscoelastic media long-wave equivalent to gas-hydrate bearing sediments are defined using an upscaling finite element method.
- The effective model predicts that variations in gas-hydrate concentration induce velocity dispersion and attenuation on P- and S- waves.

Corresponding author: Jing Ba, `jingba@188.com`

**Abstract**

Gas-hydrate bearing sediments are composite materials modeled as a porous rock frame and gas-hydrates, which consist of an ice-like lattice of water molecules with gas molecules, mostly methane, trapped inside. These type of sediments are highly heterogeneous at multiple mesoscopic scales, which induce attenuation and dispersion of traveling seismic waves due to mode conversions. This work presents a numerical upscaling procedure that allows to define a viscoelastic medium that in the average has the same behavior than the original heterogeneous sediment. The upscaling procedure consists of determining the complex moduli associated with the viscoelastic medium by solving numerically boundary value problems representing compressibility and shear experiments. The procedure is applied to composite media with regions of different ice content of fractal or periodic layered distribution. The examples demonstrate that variations in ice content induce strong attenuation and dispersion effects on seismic waves due to the WIFF mechanism.

## 1 Introduction

Gas-hydrate bearing sediments are partially frozen porous rocks containing heterogeneities at multiple mesoscopic scales. These structures consist of a water phase and two non-welded solid phases, the porous skeleton and gas-hydrates, which are ice-like lattices of water molecules with gas molecules trapped inside (Ecker et al. (2000), Guerin and Goldberg (2005)). These formations, found in permafrost and continental margins, are considered as important future energy resources (Ecker et al. (2000)). Their elastic properties and seismic velocities were analyzed by Lee and Collet (2001), Lee (2002) and Carcione and Tinivella (2000).

A theory to describe the static and dynamic behavior of partially frozen porous media was presented by Leclaire et al (1994). The theory, valid for uniform porosity, predicts the existence of additional compressional and shear waves which were observed in laboratory experiments (Leclaire et al (1995)). Carcione and Seriani (1998) designed a generalization of this theory to evaluate gas-hydrate concentration. Carcione et al. (2003) and Santos et al. (2004) generalized the theory of Leclaire et al. (1994) to the variable porosity case. Numerical simulations of wave propagation in partially frozen porous media was presented by Carcione and Seriani (2001) and Carcione et al. (2003).

Seismic waves traveling through partially frozen porous media with regions of different ice content suffer mode conversions at interfaces between those regions, generating wave-induced fluid flow (WIFF) in what it is known as the mesoscopic loss mechanism. This mechanism was first analyzed by White et al. (1975) for the case of layered porous rocks with alternating gas and water saturation.

Eventhough the generalized theory of Leclaire could in principle be used to simulate wave propagation in highly heterogeneous gas-hydrate bearing sediments, large linear systems of equations need to be solved to properly represent the heterogeneities As an alternative, this work proposes the use of a numerical upscaling procedure allowing to obtain an *effective viscoelastic isotropic medium* (EVIM) that in the average behaves as a highly heterogeneous gas-hydrate bearing sediment.

The complex moduli that determine the EVIM are obtained as solutions of two boundary value problems (BVP's) for the quasistatic equations for composite materials derived by Santos et al. (2004). The BVP's impose boundary conditions associated with compressibility and shear experiments which approximate solution is obtained using a Finite Element (FE) procedure.

For a detailed description of using harmonic experiments combined with FE procedures to determine the seismic response of Biot-type media with different types of heterogeneities we refer to Santos and Gauzellino (2017).

## 2 The differential model

Let us consider an elementary cube $\Omega$ composed of two weakly-coupled porous solid phases, referred to by the subscripts or superscripts 1 and 3, saturated by a single-phase fluid phase indicated by the subscript or superscript 2. Thus, $\Omega = \Omega_1 \cup \Omega_2 \cup \Omega_3$. The water content (effective porosity) and the two solid fractions over the bulk material are defined as $\phi_w = \dfrac{V_2}{V_b}$, $\phi_1 = \dfrac{V_1}{V_b}$ and $\phi_3 = \dfrac{V_3}{V_b}$, respectively, where $V_b = V_1 + V_2 + V_3$ and $V_i$ is the volume of the phase $\Omega_i$. The absolute porosity $\phi_a$, corresponding to the case when the porous rock is completely unfrozen is $\phi_a = \phi_w + \phi_3 = 1 - \phi_1$.

The ice content $I'$ is defined as $I' = \dfrac{\phi_3}{1-\phi_w}$, so that $0 \le I' \le 1$.

Let $\boldsymbol{\tau}^{(1,T)} = (\tau_{jk}^{(1,T)})$ and $\boldsymbol{\tau}^{(3,T)} = (\tau_{jk}^{(3,T)})$ denote the stress tensors in $\Omega_1$ and $\Omega_3$ averaged over the bulk material $\Omega$, respectively, and let $p_f$ denote the fluid pressure. Also, let $\mathbf{u}^{(1)}$, $\mathbf{u}^{(2)}$ and $\mathbf{u}^{(3)}$ be the averaged solid and fluid displacements over the bulk material, while the relative fluid displacement is defined as

$$\mathbf{w} = \phi_w\big(\mathbf{u}^{(2)} - S_1\mathbf{u}^{(1)} - S_3\mathbf{u}^{(3)}\big), \tag{1}$$

with $S_1 = \dfrac{V_1}{V_1+V_3}, S_3 = \dfrac{V_3}{V_1+V_3}$ and $\zeta = -\nabla\cdot\mathbf{w}$ representing the change in fluid content. Furthermore, let

$$\epsilon_{ij}(u^{(m)}) = \frac{1}{2}\left(\frac{\partial u_i^{(m)}}{\partial x_j} + \frac{\partial u_j^{(m)}}{\partial x_i}\right), \quad m = 1, 3,$$

denote the strain tensor in $\Omega_m$ with linear invariant $\theta_m = \epsilon_{ii}(u^{(m)})$.

The diffusive equations for a partially frozen porous medium are (Santos et al. (2004))

$$\mathrm{i}\omega \mathrm{f}_{11}\mathbf{u}^{(1)} - \mathrm{i}\omega \mathrm{f}_{12}\mathbf{u}^{(2)} - \mathrm{i}\omega \mathrm{f}_{11}\mathbf{u}^{(3)} = \nabla\cdot\boldsymbol{\tau}^{(1,\mathrm{T})}, \tag{2}$$
$$-\mathrm{i}\omega \mathrm{f}_{12}\mathbf{u}^{(1)} + \mathrm{i}\omega \mathrm{f}_{22}\mathbf{u}^{(2)} + \mathrm{i}\omega \mathrm{f}_{12}\mathbf{u}^{(3)} = -\nabla \mathrm{p}_{\mathrm{f}}, \tag{3}$$
$$-\mathrm{i}\omega \mathrm{f}_{11}\mathbf{u}^{(1)} + \mathrm{i}\omega \mathrm{f}_{12}\mathbf{u}^{(2)} + \mathrm{i}\omega \mathrm{f}_{11}\mathbf{u}^{(3)} = \nabla\cdot\boldsymbol{\tau}^{(3,\mathrm{T})}. \tag{4}$$

where $\omega$ is the angular frequency, $\mathrm{i} = \sqrt{-1}$ and

$$\tau_{jk}^{(1,T)} = \big[K_{G1}\theta_1 - B_1\zeta + B_3\theta_3\big]\delta_{jk} + 2\mu_1 d_{jk}^{(1)} + \mu_{1,3} d_{jk}^{(3)}, \tag{5}$$
$$\tau_{jk}^{(3,T)} = \big[K_{G3}\theta_3 - B_2\zeta + B_3\theta_1\big]\delta_{jk} + 2\mu_3 d_{jk}^{(3)} + \mu_{1,3} d_{jk}^{(1)},\ j,k = 1,2,3, \tag{6}$$
$$p_f = -B_1\theta_1 - B_2\theta_3 + M\zeta, \tag{7}$$

See Santos et al. (2004), Appendices A and B to find a procedure to determine the elastic coefficients in equations (5)–(7) and the diffusive coefficients $f_{11}, f_{22}$ and $f_{12}$ in equations (2)-(4).

## 3 The Finite Element upscaling procedure

Let us denote by $\mathcal{T}(\widetilde{\mathbf{u}}^s)$ and $\mathcal{E}(\widetilde{\mathbf{u}}^s)$ the time Fourier transforms of the stress and strain tensors of the EVIM, and set $\widetilde{\Theta}^s = \nabla\cdot\widetilde{\mathbf{u}}^s$, where $\widetilde{\mathbf{u}}^s$ denotes the solid displacement vector. The constitutive equations of the EVIM are

$$\mathcal{T}_{jk}(\widetilde{\mathbf{u}}^s) = \overline{\lambda}\widetilde{\Theta}^s\delta_{jk} + 2\overline{\mu}\mathcal{E}_{jk}(\widetilde{\mathbf{u}}^s). \tag{8}$$

To determine the complex and frequency dependent moduli $\overline{E_u} = \overline{\lambda} + 2\overline{\mu}$ and $\overline{\mu}$ equations (2)-(4) are solved on a square $\Omega = (0, L)^2$ in the $(x_1, x_3)$-plane with boundary $\Gamma = \Gamma^L \cup \Gamma^B \cup \Gamma^R \cup \Gamma^T$. Here $\Gamma^L, \Gamma^R$, $\Gamma^T$ and $\Gamma^B$ denote the left, right top and

bottom boundaries of $\Gamma$. Let $\{\boldsymbol{\nu}, \boldsymbol{\chi}\}$ be an orthonormal system on $\Gamma$, where $\boldsymbol{\nu}$ the unit outer normal on $\Gamma$ and $\boldsymbol{\chi}$ be a unit tangent on $\Gamma$ oriented counterclockwise.

The complex modulus $\overline{E_u}$ is determined by solving equations (2)-(4) in $\Omega$ with the boundary conditions

$$\boldsymbol{\tau}^{(m,T)}(\mathbf{u})\boldsymbol{\nu} \cdot \boldsymbol{\nu} = -\Delta P_1, \quad (x_1, x_3) \in \Gamma^T, \quad m = 1, 3, \tag{9}$$
$$\boldsymbol{\tau}^{(m,T)}(\mathbf{u})\boldsymbol{\nu} \cdot \boldsymbol{\chi} = 0, \quad (x_1, x_3) \in \Gamma, \quad m = 1, 3, \tag{10}$$
$$\mathbf{u}^{(m)} \cdot \boldsymbol{\nu} = 0, \quad (x_1, x_3) \in \Gamma \setminus \Gamma^T, \quad m = 1, 3, \tag{11}$$
$$\mathbf{w} \cdot \boldsymbol{\nu} = 0, \quad (x_1, x_3) \in \Gamma. \tag{12}$$

Note that the solution of this BVP satisfies the relations

$$\epsilon_{11}(\mathbf{u}^{(1)}) = \epsilon_{13}(\mathbf{u}^{(1)}) = \epsilon_{11}(\mathbf{u}^{(3)}) = \epsilon_{13}(\mathbf{u}^{(3)}) = \nabla \cdot \mathbf{w} = 0.$$

Thus, $\mathcal{E}_{11}(\widetilde{\mathbf{u}}^s) = \mathcal{E}_{13}(\widetilde{\mathbf{u}}^s) = 0$ and (8) reduces to

$$\mathcal{T}_{33} = \overline{E_u}\mathcal{E}_{33}. \tag{13}$$

Now $\overline{E_u}$ can be determined from (13) by obtaining $\mathcal{T}_{33}$ and $\mathcal{E}_{33}$ as averages of the mesoscopic stress and strain tensors associated with the solid 1 phase over the sample $\Omega$, i.e.,

$$\mathcal{T}_{33} = \frac{1}{\Omega}\int_\Omega \tau_{33}^{(1,T)} d\Omega, \qquad \mathcal{E}_{33} = \frac{1}{\Omega}\int_\Omega \epsilon_{33}^{(1)} d\Omega. \tag{14}$$

Next, the complex shear modulus $\overline{\mu}$ is determined by solving (2)-(4) in $\Omega$ with the boundary conditions

$$-\boldsymbol{\tau}^{(1,T)}(\mathbf{u})\boldsymbol{\nu} = \mathbf{g}_1, \quad (x_1, x_3) \in \Gamma^T \cup \Gamma^L \cup \Gamma^R, \tag{15}$$
$$-\boldsymbol{\tau}^{(3,T)}(\mathbf{u})\boldsymbol{\nu} = \mathbf{g}_3, \quad (x_1, x_3) \in \Gamma^T \cup \Gamma^L \cup \Gamma^R, \tag{16}$$
$$\mathbf{u}^{(m)} = 0, \quad (x_1, x_3) \in \Gamma^B, \quad m = 1, 3 \tag{17}$$
$$\mathbf{w} \cdot \nu = 0, \quad (x_1, x_3) \in \Gamma, \tag{18}$$

where

$$\mathbf{g}_1 = \begin{cases} (0, \Delta G_1), & (x_1, x_3) \in \Gamma^L, \\ (0, -\Delta G_1), & (x_1, x_3) \in \Gamma^R, \\ (-\Delta G_1, 0), & (x_1, x_3) \in \Gamma^T, \end{cases} \tag{19}$$

$$\mathbf{g}_3 = \begin{cases} (0, \Delta G_3), & (x_1, x_3) \in \Gamma^L, \\ (0, -\Delta G_3), & (x_1, x_3) \in \Gamma^R, \\ (-\Delta G_3, 0), & (x_1, x_3) \in \Gamma^T. \end{cases} \tag{20}$$

The solution of this BVP satisfies the conditions

$$\epsilon_{11}(\mathbf{u}^{(1)}) = \epsilon_{33}(\mathbf{u}^{(1)} = \epsilon_{11}(\mathbf{u}^{(3)}) = \epsilon_{33}(\mathbf{u}^{(3)} = \nabla \cdot \mathbf{w} = 0,$$

and consequently $\mathcal{E}_{11}(\widetilde{\mathbf{u}}^s) = \mathcal{E}_{33}(\widetilde{\mathbf{u}}^s) = 0$. Hence, (8) reduces to

$$\mathcal{T}_{13} = \overline{\mu}\mathcal{E}_{13}. \tag{21}$$

Now $\overline{\mu}$ is obtained from (21) by computing $\mathcal{T}_{13}$ and $\mathcal{E}_{13}$ averaging the mesoscopic stress and strain tensors associated with the solid 1 phase over the sample $\Omega$:

$$\mathcal{T}_{13} = \frac{1}{\Omega}\int_\Omega \tau_{13}^{(1)} d\Omega, \qquad \mathcal{E}_{13} = \frac{1}{\Omega}\int_\Omega \epsilon_{13}^{(1)} d\Omega. \tag{22}$$

The average bulk density of the sample $\overline{\rho}$ is

$$\overline{\rho} = \phi_1\rho_1 + \phi_w\rho_2 + \phi_3\rho_3,$$

with $\rho_m, m = 1, 2, 3$ denoting the mass density of each solid and fluid constituent in $\Omega$. The complex compressional and shear velocities are (Carcione, 2014)

$$v_{Pc}(\omega) = \sqrt{\frac{\overline{E_u}(\omega)}{\overline{\rho}}}, \quad v_{Sc}(\omega) = \sqrt{\frac{\overline{\mu}(\omega)}{\overline{\rho}}}.$$

The effective P and S phase velocities $v_n(\omega)$ and (inverse) quality factor $Q_n(\omega), n = P, S$ are determined using the relations (Carcione, 2014)

$$v_n(\omega) = \left[\mathrm{Re}\left(\frac{1}{v_{nc}(\omega)}\right)\right]^{-1}, \qquad \frac{1}{Q_n(\omega)} = \frac{\mathrm{Im}(v_{nc}(\omega)^2)}{\mathrm{Re}(v_{nc}(\omega)^2)}, \quad n = P, S. \tag{23}$$

The approximate solution (2)-(4) with the boundary conditions (9)–(12) to determine $\overline{E_u}$ and and (15)– (18) to determine $\overline{\mu}$ was obtained using the FE procedure described in Appendix B.

## 4 Numerical experiments

To validate the procedure, we consider a water saturated homogeneous square sample of side length 10 cm discretized using a $80 \times 80$ uniform mesh. Absolute porosity is $\phi_a = 0.3$. The material properties of solid 1, solid 3 (ice) and water are given in Table 1.

The effective phase velocities $v_n$ and dissipation factors $1000/Q_n$, $n = P, S$ obtained using the harmonic experiments for the composite model were validated by comparison against those corresponding to the associated classic Biot model defined in Appendix A and using plane-wave analysis.

### 4.1 Validation varying ice content at 50 Hz and varying frequency for ice content $I' = 0.333$

Table 2 shows the results for the effective P-wave phase velocities at 50 Hz varying the ice content. Its comparison with the values of the associated classic Biot model is displayed in the column of the percentual error. The error decreases with decreasing ice content. We consider that this is due to the very different elastic behavior of the solid 1 and solid 3 (ice) phases.

Furthermore, the effective P-wave velocities as a function of frequency for ice content $I'$=0.333 were computed in the range 1 Hz–1 kHz. We obtained an effective P-wave velocity of 3992.67 m/s and numerical $\infty$ for the quality factor $Q$. We also computed the P-wave velocity for the associated classic Biot model defined in Appendix A using a plane-wave analysis, obtaining a constant of 4087.86 and dissipation factors in the range $10^{-2}$–$10^{-5}$.

An analog to Table 2 is presented in the Table 3 for the results of the effective S-wave phase velocities.

Table 3 shows that, as for P-waves, errors decrease with decreasing ice content. We also computed the effective S-wave velocities as a function of frequency for ice content $I'$=0.333. In the frequency range 1 Hz–1 kHz we obtained an effective S-wave velocity of 2476.96 m/s and numerical $\infty$ for the shear quality factor $Q$. The plane-wave analysis for the associated classical Biot model gives an S-wave phase velocity of 2477.85 m/s, while the dissipation factors are in the range $10^{-2} - 10^{-5}$.

## 5 Effective P-wave phase velocity and dissipation factors in layered media with periodic variations in ice content $I'$

We consider a square sample of side length 18 cm size discretized with a $120 \times 120$ uniform mesh. The numerical sample has seven alternating layers of ice contents $I' = 0.666$ and $I' = 0.166$. Absolute porosity is $\phi_a = 0.3$.

To determine the FE approximations to the the plane wave modulus $\overline{E_u}(\omega)$, we solved the diffusive equations (2) – (4) with the boundary conditions (9)–(12) using the FE method for frequencies in the range 1 Hz- 200 Hz.

The curves labeled *Associated classic Biot, theory* in Figures 1 and 2 were obtained as follows. First we determined the associated classic Biot model for each layer of the periodic sequence as indicated in Appendix A. Then, we use the theory presented by Krzikalla and Müller (2011) to obtain the theoretical values.

Figure 1 exhibits effective P-wave phase velocities for the composite model increasing with increasing, while those of the associated classic Biot model are almost constant in the whole frequency range. Furthermore, for almost all frequencies the composite model exhibits lower effective velocities than the classic model, due to the high dispersion induced by the WIFF mechanism. Figure 2 displays the effective dissipation factor of the composite model, where it can be observed high attenuation of P-waves due to the interlayer WIFF mechanism, with an attenuation peak of quality factor $Q = 80$ at about 70 Hz. Figure 3 displays the logarithm of the dissipation factor for the composite and associated classic Biot models, where attenuation is negligible for the associated classic Biot model.

Figures 4 and 5 show the gradient of fluid pressure for this experiment at 10 Hz and 70 Hz, where their higher values can be observed at the interlayer boundaries and are due to variations in ice content in the sample. These Figures illustrates the WIFF mechanism. Furthermore, these gradients are much higher at 70 Hz than at 10 Hz, in accordance with Figure 2.

## 6 Patchy ice-content.

Gas-hydrate bearing sediments have local variations in ice content $I'$ at multiple mesoscopic scales. To model wave propagation in this type of medium, a convenient approach is to use an EVIM as defined in the previous sections. This EVIM takes into account the WIFF and the associated dispersion and attenuation effects.

The water-saturated sample $\Omega$ is a square of side length 10 cm and is discretized with a $80 \times 80$ uniform mesh.

The binary multiscale binary quasi-fractal heterogeneities in ice content were generated using the von Karman self-similar correlation function (Frankel and Clayton (1986)). The examples used fractal dimension $D$ =2.2 and two correlation lengths, 3.33 cm and 2.22 cm, respectively, For details on the procedure to construct these type of fractal distributions we refer to Santos and Gauzellino (2017).

Figures 6 and 7 display the patchy ice content distribution $I'$ for correlation lengths 3.33 cm and 2.22 cm, respectively. Overall ice content $I'$ is 36 %. Figure 8 shows the Lamé shear coefficient $\mu_1$ associated with the patchy ice content distribution $I'$ in Figure 6, where the local heterogeneities in $\mu_1$ are due to the local variations in ice content. Figures 9 and 10 show effective phase velocities and logarithm of the dissipation factors of P-waves as a function of frequency for the composite and associated classic Biot models in the range 0.01 Hz–140 Hz and binary ice content $I'$ as in Figure 6 (correlation length 3.33 cm). The results for the associated classic Biot model were obtained using the FE upscaling procedure presented by Santos et al. (2009).

As in the periodic layered case, P-wave velocities for the composite model are lower than those of the associated classic Biot model, show highly dispersive behavior and higher values with increasing frequency, while those of the associated classic Biot model are almost constant in all the frequency range.

Figure 10 shows that attenuation of P-waves is much higher for the composite model than for the associated classic Biot model. This attenuation mechanism, due to the induced WIFF effect, is not present when the associated classic Biot model is used. Figure 11 exhibits dissipation factors as a function of frequency for the harmonic composite model and the binary ice content distributions in Figures 6 and 7. Two attenuation peaks are clearly observed. The peak located at low frequencies corresponds to the larger ice patches (Figure 6).

The last experiment analyzes the behavior of effective shear waves as a function of frequency due to variations in ice content. In this case, the sample is a square of side length 1 cm with a multiscale quasi-fractal patchy ice content distribution. The patches have ice content $I' = 0.666$ and $I' = 0.166$. Absolute porosity is $\phi_a = 0.3$, correlation length is 0.04 cm and fractal dimension is $D = 2.2$. Overall ice content is 41 %. Figure 12 displays the shear Lamé coefficient associated with this quasi-fractal ice content distribution. It is observed that S-waves suffer very little velocity dispersion, as can be seen in Figure 13, and negligible attenuation. We also computed the corresponding effective phase velocity and dispersion coefficient of the associated classic Biot model, obtaining a constant shear phase velocity of 2428 m/s and negligible attenuation.

## 7 Conclusions

The numerical upscaling procedure presented in this work determines effective complex and frequency dependent P- and S- wave moduli associated with a heterogeneous gas-hydrate bearing poroelastic medium. These moduli define an effective viscoelastic isotropic medium that behaves in the average as the heterogeneous gas-hydrate bearing medium. The methodology is applied to analyze the seismic response of water saturated poroelastic samples for the cases of periodic alternating layers or patches of different ice content. The analysis shows that local variations in ice content induce high velocity dispersion and attenuation for P- waves traveling in gas-hydrate bearing sediments, while S-waves are less sensitive to these type of heterogeneities.

## 8 Appendix A

In this appendix, we explain a procedure to determine the elastic and dissipative factors of an associated classic Biot model that in the low-frequency range is *equivalent* to a composite material. The following notation is used to define the associated classical Biot model (Biot, 1962).

The solid and fluid displacement particle displacements are denoted as $\widehat{\mathbf{u}}^{(s)}, \widehat{\mathbf{u}}^{(f)}$, while $\widehat{\boldsymbol{\sigma}}$ and $\widehat{p}_f$ denote the total stress and fluid pressure.

The constitutive relations and the diffusion equation of the classic Biot model are

$$\widehat{\sigma}_{ij} = \left[K_G\widehat{\theta}^{(s)} - B\widehat{\theta}^{(f)}\right]\delta_{ij} + 2\mu\widehat{d}_{ij}^{(s)}, \tag{24}$$

$$\widehat{p}_f = -B\widehat{\theta}^{(s)} - \widehat{M}\widehat{\theta}^{(f)}, \tag{25}$$

$$\nabla\cdot\widehat{\boldsymbol{\sigma}} = 0, \tag{26}$$

$$i\omega\frac{\eta}{\widehat{\kappa}}\widehat{\mathbf{u}}^{(f)} + \nabla p_f = 0, \tag{27}$$

where

$$\widehat{d}_{ij}^{(s)} = \epsilon_{ij}(\widehat{\mathbf{u}}^{s})) - \frac{1}{3}\widehat{\theta}^{(s)}\delta_{ij}, \quad \widehat{\theta}^{(m)} = \nabla\cdot\widehat{\mathbf{u}}^{(m)}, m = s, f.$$

In (24)- (27), $K_G$ and $\mu$ are the bulk and shear moduli of the saturated material, while $B$ and $\widehat{M}$ are elastic coupling coefficients. Furthermore, $\widehat{\kappa}$ denotes the porous rock permeability.

Assume that $\mathbf{u}^{(1)} = \mathbf{u}^{(3)} \equiv \mathbf{u}^{(s)}$ (the low-frequency assumption is used here) and define the total stress tensor as

$$\tau_{ij} = \tau_{ij}^{(1,T)} + \tau_{ij}^{(3,T)}. \tag{28}$$

Then adding (5) and (6), we obtain

$$\begin{aligned} \tau_{ij} &= \big[ (K_{G1} + K_{G3} + 2\ B_3)\, \theta^{(s)} - (B_1 + B_2)\, \theta^{(f)}]\delta_{ij} \qquad (29)\\ &\quad +2\,(\mu_1 + \mu_3\mu_{13})\, d_{ij}^{(s)}, \\ p_f &= -(B_1 + B_2)\theta(s) - M\theta(f), \qquad (30) \end{aligned}$$

Now from (24), (25) and (29), (30), we can identify the elastic coefficients of the associated classic Biot model as follows:

$$\begin{aligned} K_G &= K_{G1} + K_{G3} + 2\ B_3, \qquad (31)\\ B &= B_1 + B_2, \qquad (32)\\ \mu &= \mu_1 + \mu_3 + \mu_{13}, \qquad (33)\\ \widehat{M} &= M. \qquad (34) \end{aligned}$$

The procedure to determine the coefficients $K_G, B, \widehat{M}$ and $\mu$ in (31)- (34) can be shown to give identical results than when they are computed as presented in Carcione et al. (2005).
.

Furthermore, from equation (B5) and (B8) in Santos et al. (2004)

$$\begin{aligned} \phi\,(S_3\phi f_{22} - f_{12}) &= b_{23}, \qquad (35)\\ \phi\,(f_{12} + S_1\phi f_{22}) &= b_{12}, \qquad (36) \end{aligned}$$

where

$$b_{12} = \phi^2 \frac{\eta}{\kappa_1}, \qquad b_{23} = \phi^2 \frac{\eta}{\kappa_3}, \tag{37}$$

Thus, multiply by $\phi$ equations (35) and (36) and add the resulting equations to get

$$f_{22} = \eta \left( \frac{1}{\kappa_1} + \frac{1}{\kappa_3} \right). \tag{38}$$

Next, from the low-frequency assumption, the $f_{12}$-terms in (3) cancel and this equation reduces to

$$i\omega f_{22}\mathbf{u}^{(2)} + \nabla p_f = 0. \tag{39}$$

Thus (27), (38) and (39) allow to identify the *effective* permeability $\widehat{\kappa}$ of the associated classic Biot model by the relation

$$\frac{1}{\widehat{\kappa}} = \left( \frac{1}{\kappa_1} + \frac{1}{\kappa_3} \right). \tag{40}$$

Equations (31)-(34) and (40) completely define the associated classic Biot media to our composite material.

**Remark:** Equations (31)-(34) and (40) may also be used in the case of shaley sandstones as presented in Santos et al. (2004).

# 9 Appendix B

# 10 Finite element formulation

Let $\mathcal{T}^h(\Omega)$ be a non-overlapping partition of $\Omega$ into rectangles $\Omega_j$ of diameter bounded by $h$ such that $\overline{\Omega} = \cup_j^J \overline{\Omega}_j$. Denote by $\Gamma_{jk} = \partial\Omega_j \cap \partial\Omega_k$ the common side of two adjacent rectangles $\Omega_j$ and $\Omega_k$. Also, let $\Gamma_j = \partial\Omega_j \cap \Gamma$.

To approximate the solid displacements $\mathbf{u}^{(1)}$ $\mathbf{u}^{(3)}$ we use the spaces $\mathcal{W}^{h,P}(\Omega)$ (resp. $\mathcal{W}^{h,S}(\Omega)$) of vector polynomials $\mathbf{v}$ such that each component is globally continuous piecewise bilinear polynomials and also satify the condition $\mathbf{v}\cdot\boldsymbol{\nu} = 0$ on $\Gamma\backslash\Gamma^T$ (resp. $\mathbf{v} = 0$ on $\Gamma^B$).

To approximate the fluid displacement vector $\mathbf{u}^{(2)}$ we use the vector part of the Raviart-Thomas-Nedelec space of zero order (Raviart and Thomas (1977), Nedelec (1980)). This space is denoted as $\mathcal{V}^h(\Omega)$ and consists of vector polynomials having global divergence in $L^2(\Omega)$ and such that on each element $\Omega_j$ are of the form $P_{1,0}(\Omega_j) \times P_{0,1}(\Omega_j)$. Here $P_{1,0}(\Omega_j)$ denotes the polynomials linear in $x_1$ and constant in $x_3$ in $\Omega_j$, and $P_{0,1}(\Omega_j)$ those that are constant in $x_1$ and linear in $x_3$ in $\Omega_j$.

Next, for $(I) = (P, S)$ let

$$\mathcal{Z}^{h,I}(\Omega) = \mathcal{W}^{h,I}(\Omega) \times \mathcal{V}^h(\Omega) \times \mathcal{W}^{h,I}(\Omega).$$

Let $(\cdot,\cdot)_X$ and $\langle\cdot,\cdot\rangle_{\partial X}$ denote the complex $L^2(X)$ and $L^2(\partial X)$ inner products for scalar, vector, or matrix valued functions, with the subscript $X$ being omitted if $X = \Omega$ or $X = \Gamma$. Let us define the bilinear form

$$\begin{aligned}
\mathcal{L}(\mathbf{u},\mathbf{v}) = & \,\mathrm{i}\omega\left(\mathrm{f}_{11}\mathbf{u}^{(1)} - \mathrm{f}_{12}\mathbf{u}^{(2)} - \mathrm{f}_{11}\mathbf{u}^{(3)}, \mathbf{v}^{(1)}\right) \\
& + \mathrm{i}\omega\left(-\mathrm{f}_{12}\mathbf{u}^{(1)} + \mathrm{f}_{22}\mathbf{u}^{(2)} + \mathrm{f}_{12}\mathbf{u}^{(3)}, \mathbf{v}^{(2)}\right) \\
& + \mathrm{i}\omega\left(-\mathrm{f}_{11}\mathbf{u}^{(1)} + \mathrm{f}_{12}\mathbf{u}^{(2)} + \mathrm{f}_{11}\mathbf{u}^{(3)}, \mathbf{v}^{(3)}\right) \\
& + \sum_{pq}\left(\tau_{pq}^{(1,T)}(\mathbf{u}),\, \varepsilon_{pq}(\mathbf{v}^{(1)})\right) - \left(p_f(\mathbf{u}), \nabla\cdot\mathbf{v}^{(2)}\right) \\
& + \sum_{pq}\left(\tau_{pq}^{(3,T)}(\mathbf{u}),\, \varepsilon_{pq}(\mathbf{v}^{(3)})\right).
\end{aligned}$$

To determine $\overline{E_u}(\omega)$ we solve the following problem: find $\mathbf{u}^{(h,P)} \in \mathcal{Z}^{h,P}(\Omega)$ such that

$$\mathcal{L}(\mathbf{u}^{(h,P)}, \mathbf{v}) = -\left\langle \Delta P_1, \mathbf{v}^{(1)}\cdot\boldsymbol{\nu}\right\rangle_{\Gamma^T} - \left\langle \Delta P_3, \mathbf{v}^{(3)}\cdot\boldsymbol{\nu}\right\rangle_{\Gamma^T}, \;\forall\, \mathbf{v} \in \mathcal{Z}^{h,P}(\Omega). \quad (41)$$

Similarly, to determine $\overline{\mu}(\omega)$ we solve the problem: find $\mathbf{u}^{(h,S)} \in \mathcal{Z}^{h,S}(\Omega)$ such that

$$\mathcal{L}(\mathbf{u}^{(h,S)}, \mathbf{v}) = \left\langle \mathbf{g}_1, \mathbf{v}^{(1)}\right\rangle_{\Gamma\backslash\Gamma^B} + \left\langle \mathbf{g}_3, \mathbf{v}^{(3)}\right\rangle_{\Gamma\backslash\Gamma^B}, \qquad \forall\, \mathbf{v} \in \mathcal{Z}^{h,S}(\Omega), \qquad (42)$$

where $\mathbf{g}_1$ and $\mathbf{g}_3$ are defined in (19)-(20). The error associated with the FE procedures (41) and (42) is on the order $O(h^{1/2})$ in the energy norm (Santos and Carcione (2015)).

**Acknowledgments**

This work was partially funded by ANPCyT, Argentina (PICT 2015 1909) and Universidad de Buenos Aires (UBACyT 20020160100088BA).

## References


Biot, M. A. (1962). Mechanics of deformation and acoustic propagation in porous media. *Journal of Applied Physics*, 33, 1482-1498.

Carcione, J. M., & Seriani, G. (1998). Seismic velocities in permafrost. *Geophysical Prospecting*, 46 441–454.

Carcione, J. M., & Tinivella, U. (2000). Bottom-simulating reflectors: Seismic velocities and AVO effects. *Geophysics*, 65 (1) 54-67.

Carcione, J. M., & Seriani, G. (2001). Wave simulation in frozen porous media. *Journal of Computational Physics*, 170, 676-695.

Carcione, J. M., Santos, J. E., Ravazzoli, C. L., & Helle, H. B. (2003). Wave simulation in partially frozen porous media with fractal freezing conditions. *Journal of Applied Physics*, 94 (12) 7839-7847.

Carcione, J. M., Helle, H. B., Santos J. E., & Ravazzoli, C. L. (2005). A constitutive equation and generalized Gassmann modulus for multi-mineral porous media. *Geophysics*, 70 (2) N17–N26.

Carcione, J. M. (2014). Wave Fields in Real Media. Theory and numerical simulation of wave propa- gation in anisotropic, anelastic, porous and electromagnetic media, 3rd ed., extended and revised. Elsevier Science, Oxford.

Ecker, C., Dvorkin, J.,& Nur, A.M. (2000). Estimating the amount of gas hydrate and free gas from marine sediments. *Geophysics*, 65 (2) 565573.

Frankel, A., & Clayton, R. W. (1986). Finite difference simulation of seismic wave scattering: implications for the propagation of short period seismic waves in the crust and models of crustal heterogeneity. *Journal of Geophysical Research*, 91 6465–6489.

Guerin, G., & Goldberg, D. (2005). Modeling of acoustic wave dissipation in gas-hydrate bearing sediments. *Geochemistry, Geophysics, Geosystems*, 6 (7), doi:10.1029/2005GC000918.

Krzikalla, F., & Müller, T. M. (2011). Anisotropic P-SV-wave dispersion and attenuation due to interlayer flow in thinly layered porous rocks. *Geophysics*, 76 WA135.

Leclaire, P., Cohen-Tenoudji, F., & Aguirre Puente, J. (1994). Extension of Biots theory to wave propagation in frozen porous media. *Journal of the Acoustical Society of America*, 96 3753–3767.

Leclaire, P., Cohen-Tenoudji, F., & Aguirre Puente, J. (1995). Observation of two longitudinal and two transverse waves in a frozen porous medium. *Journal of the Acoustical Society of America*, 97 2052–2055.

Lee, M. W., & Collet, T. S. (2001). Elastic properties of gas hydrate-bearing sediments. *Geophysics*, 66 (3) 763-771.

Lee, M. W. (2002). Biot-Gassmann theory for velocities of gas hydrate-bearing sediments. *Geophysics*, 67 (6) 1711-1719.

Nedelec, J. C. (1980). Mixed finite elements in $R^3$. *Numerische . Mathematik*, 35 315-341.

Raviart, P. A., & Thomas, J. M. (1975). Mixed finite element method for 2nd order elliptic problems, Mathematical Aspects of the Finite Element Methods. *Lecture Notes of Mathematics*. 606 Springer.

Santos, J.E., Ravazzoli, C.L., & Carcione, J. M. (2004). A model for wave propagation in a composite solid matrix saturated by a single-phase fluid. *Journal of the Acoustical Society of America*, 115 (6) 2749-2760.

Santos, J. E., Ravazzoli, C. L., Gauzellino, P. M., & Carcione, J. M. (2009). A numerical upscaling procedure to estimate effective bulk and shear moduli in heterogeneous fluid-saturated porous media. *Computer Methods in Applied Mechanics and Engineering*, 198 2067-2077.

Santos, J. E., & Carcione, J. M. (2015). Finite-element harmonic experiments to model fractured induced anisotropy in poroelastic media. *Computer Methods in Applied Mechanics and Engineering*, 283 1189–1213.

Santos, J. E., & Gauzellino, P. M. (2017). *Numerical Simulation in Applied Geophysics*. Birkhauser, Lecture Notes in Geosystems Mathematics and Computing.

White, J. E., Mikhaylova, N. G., & Lyakhovitskiy, F. M. (1975). Low-frequency seismic waves in fluid saturated layered rocks. *Physics of the Solid Earth*, 11 654–659.

**Table 1. Material Properties.**

| | | |
|---|---|---|
| Solid grain | bulk modulus, $K_{s1}$ | 38.7 GPa |
| | shear modulus, $\mu_{s1}$ | 39.6 GPa |
| | density, $\rho_{s1}$ | 2650 kg/m$^3$ |
| | permeability $\kappa_{s1}$ | 1.07 $10^{-13}$ m$^2$ |
| Ice | bulk modulus, $K_{s3}$ | 8.58 GPa |
| | shear modulus, $\mu_{s3}$ | 3.32 GPa |
| | density, $\rho_{s3}$ | 920 kg/m$^3$ |
| | permeability $\kappa_{s3}$ | 5 $10^{-4}$ m$^2$ |
| Water | bulk modulus, $K_f$ | 2.25 GPa |
| | density, $\rho_2$ | 1040 kg/m$^3$ |
| | viscosity, $\eta$ | 0.0018 Pa $\cdot$ $s$ |

**Table 2. Effective P-wave velocities (m/s) at 50 Hz as function of ice content $I'$. The sample is square of side length 10 cm.**

| Ice content $I'$ | Composite model | Associated classic Biot model | Error (%) |
|---|---|---|---|
| 0.666 | 4120.23 | 4291.95 | 4.0 |
| 0.583 | 4064.1868 | 4208.35 | 3.42 |
| 0.500 | 4027.02 | 4146.20 | 2.87 |
| 0.416 | 4004.44 | 4100.76 | 2.34 |
| 0.333 | 3992.67 | 4067.86 | 1.85 |
| 0.25 | 3988.476 | 4043.88 | 1.37 |
| 0.166 | 3989.24 | 4025.78 | 0.9 |

**Table 3. Effective S-wave phase velocities (m/s) at 50 Hz as function of ice content $I'$. The sample is square of side length 10 cm.**

| Ice content $I'$ | Composite model | Associated classic Biot model | Error (%) |
|---|---|---|---|
| 0.666 | 2627.56 | 2639.26 | 0.44 |
| 0.583 | 2627.56 | 2572.3665 | 0.28 |
| 0.500 | 2565.15 | 2526.03 | 0.16 |
| 0.416 | 2493.87 | 2495.93 | 0.08 |
| 0.333 | 2476.96 | 2477.85 | 0.03 |
| 0.25 | 2467.65 | 2467.95 | 0.01 |
| 0.166 | 2462.93 | 2462.99 | 0.0 |

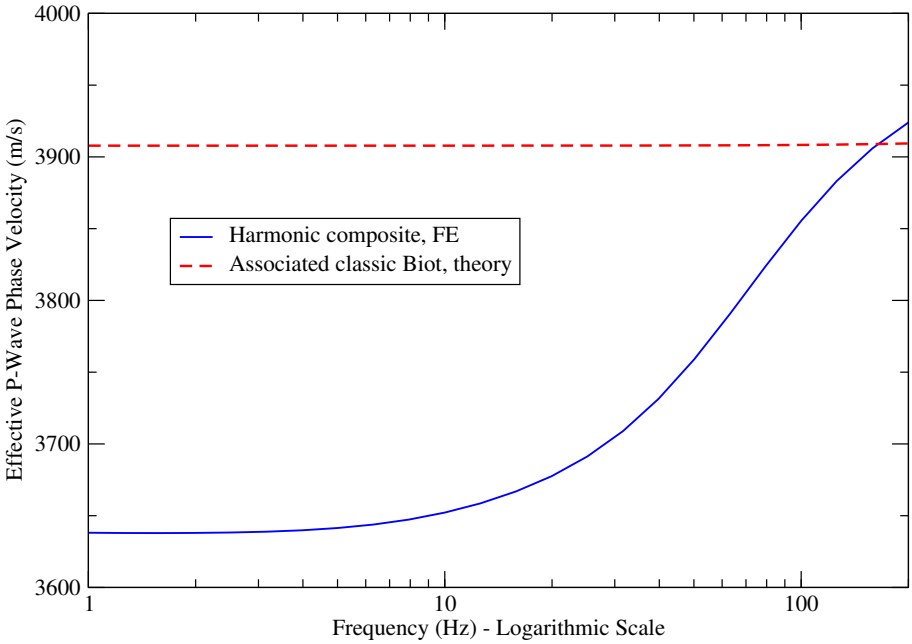


**Figure 1.** Effective P-wave phase velocity as a function of frequency for the composite and associated classic Biot models. The numerical sample is a square of side length 18 cm and has seven alternating layers of ice contents $I' = 0.666$ and $I' = 0.166$.

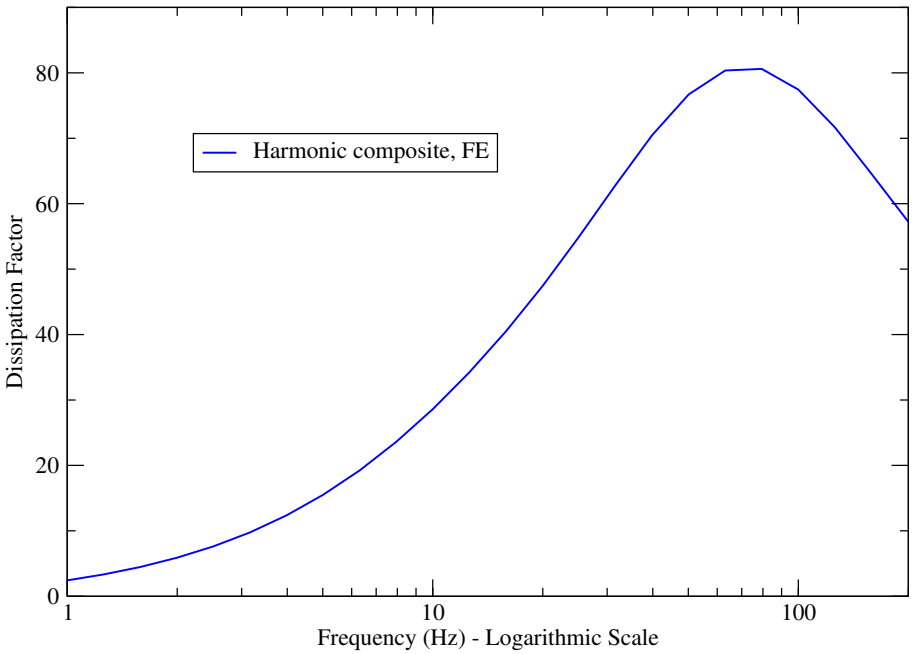


**Figure 2.** Effective P-wave dissipation factor as a function of frequency for the composite model. The numerical sample is a square of side length 18 cm and has seven alternating layers of ice contents $I' = 0.666$ and $I' = 0.166$.

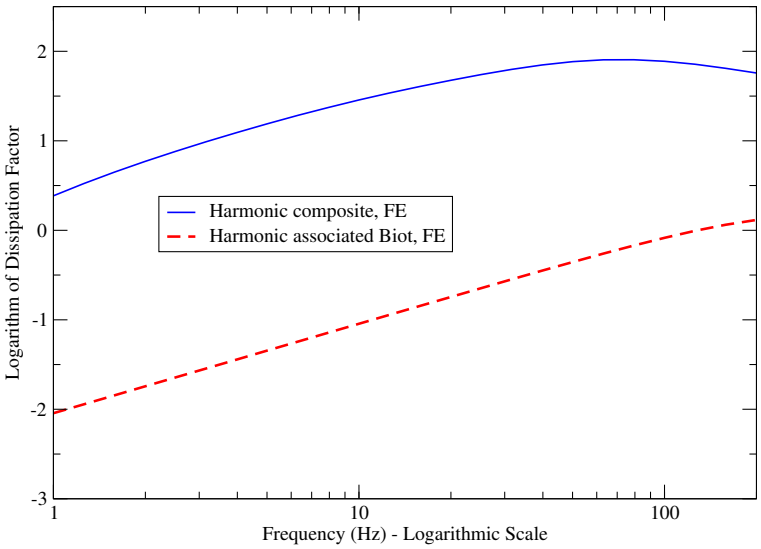


**Figure 3.** Logarithm of the effective P-wave dissipation factor as a function of frequency for the composite and associated classic Biot models. The numerical sample is a square of side length 18 cm and has seven alternating layers of ice content $I' = 0.666$ and $I' = 0.166$.

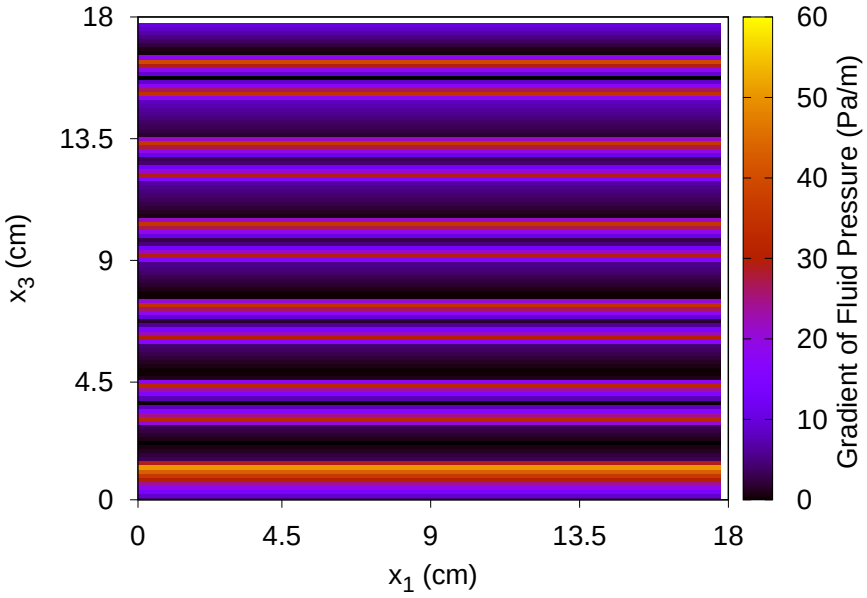


**Figure 4.** Gradient of fluid pressure at 10 Hz for a square numerical sample of side length 18 cm and with seven alternating layers of ice contents $I' = 0.666$ and $I' = 0.166$.

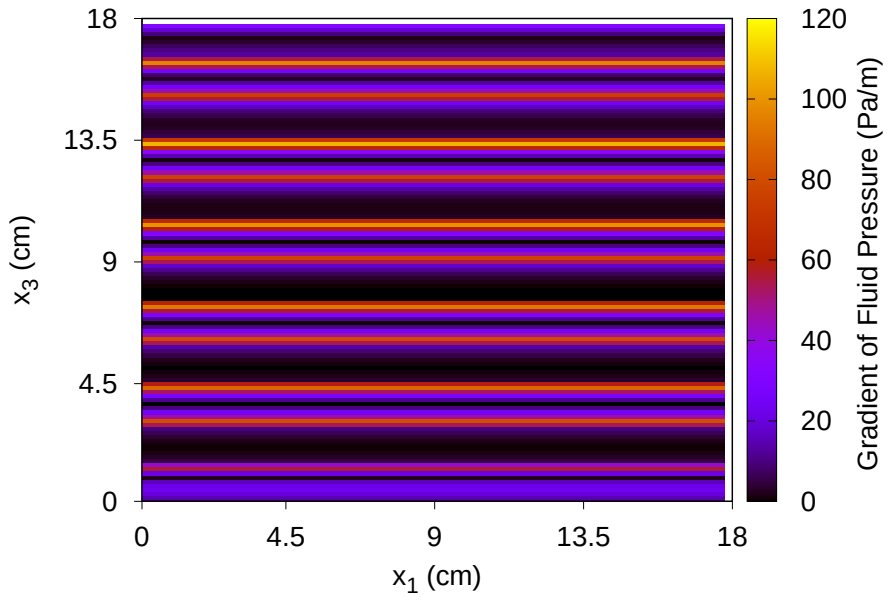


**Figure 5.** Gradient of fluid pressure at 70 Hz for a square numerical sample of side length 18 cm with seven alternating layers of ice contents $I' = 0.666$ and $I' = 0.166$.

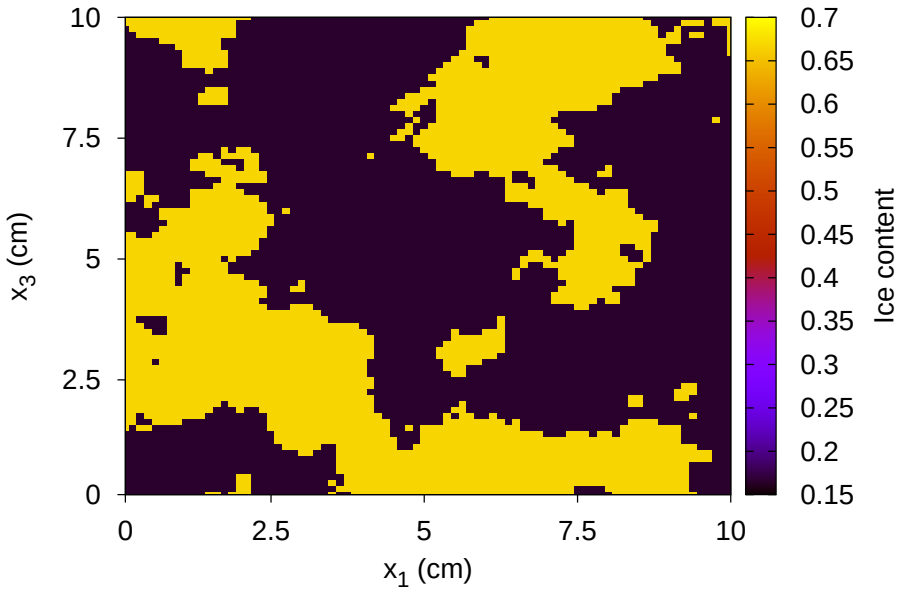


**Figure 6.** Binary patchy ice content $I'$. Black regions have $I' = 0.666$, yellow regions have $I' = 0.166$. Absolute porosity $\phi_a = 0.3$. Correlation length is 3.33 cm, fractal dimension is is $D = 2.22$. Overall ice content is 36 %. The sample is a square of side length 10 cm.

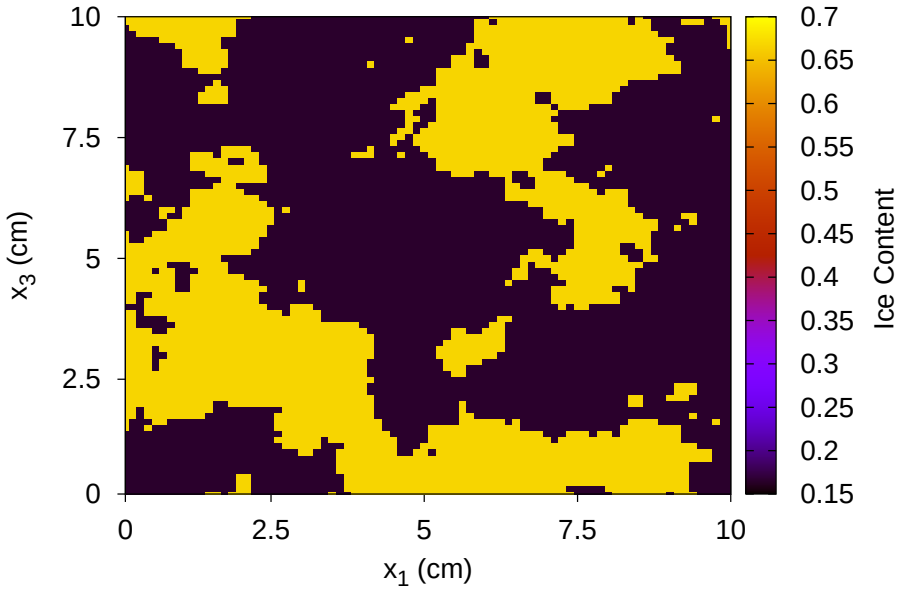


**Figure 7.** Binary patchy ice content $I'$. Black regions have $I' = 0.666$, yellow regions have $I' = 0.166$. Absolute porosity $\phi_a = 0.3$. Correlation length is 2.22 cm and fractal dimension is $D = 2.2$. Overall ice content is 36 %. The sample is a square of side length 10 cm.

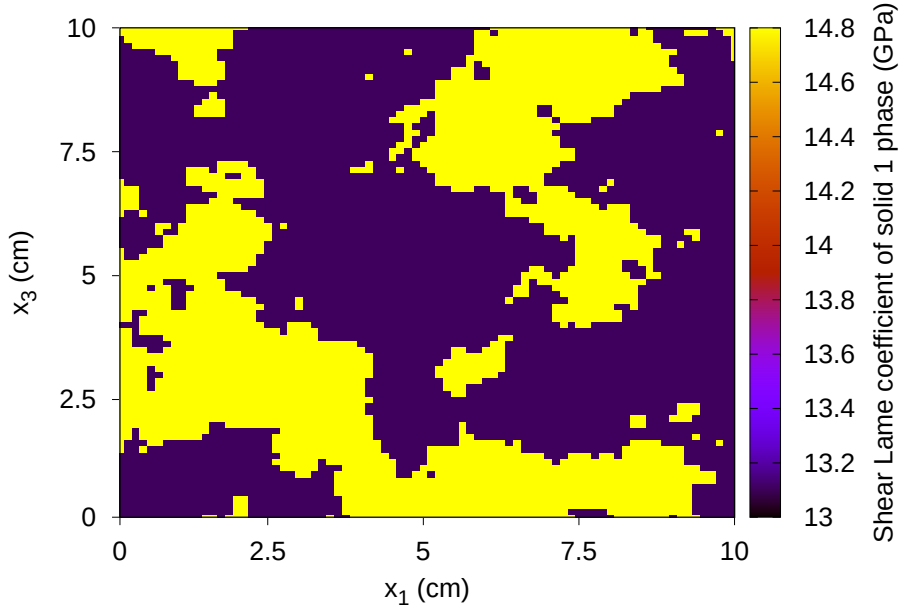


**Figure 8.** Lamé shear coefficient $\mu_1$ associated with the binary patchy ice content of correlation length 2.22 cm and and fractal dimension is $D = 2.2$ Overall ice content is 36 %. The sample is a square of side length 10 cm.

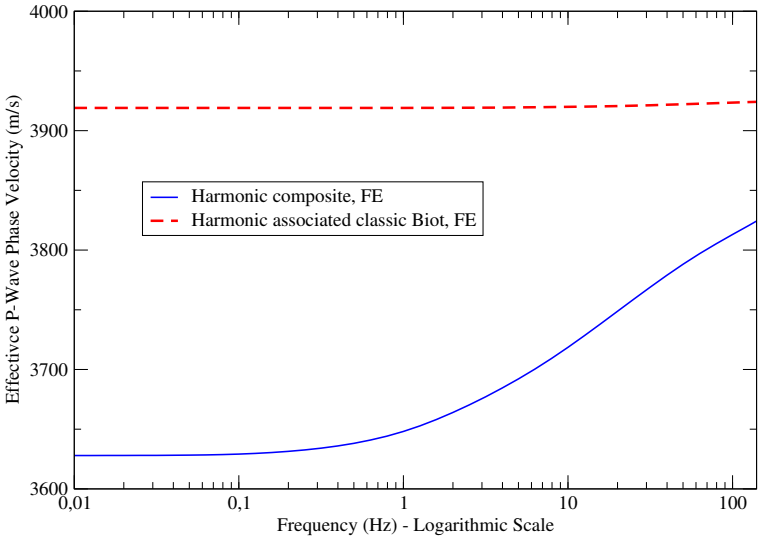


**Figure 9.** Effective P-wave phase velocity as a function of frequency for the composite and associated classic Biot models and fractal binary ice content $I'$ as in Figure 7. Correlation length is 2.22 cm and Overall ice content is 36 %. The sample is a square of side length 10 cm.

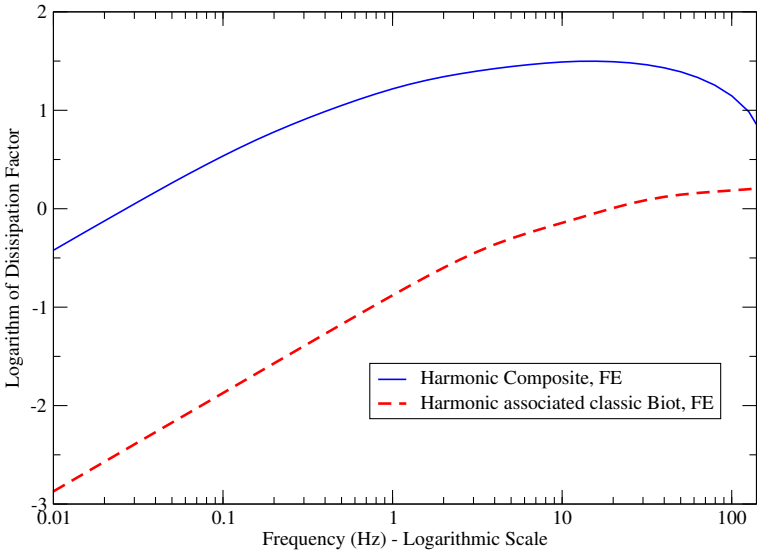


**Figure 10.** Effective P-wave dissipation factor as a function of frequency for the composite and associated classic Biot models and fractal binary ice content $I'$ as in Figure 7. Correlation length is 2.22 cm and Overall ice content is 36 %. The sample is a square of side length 1 cm.

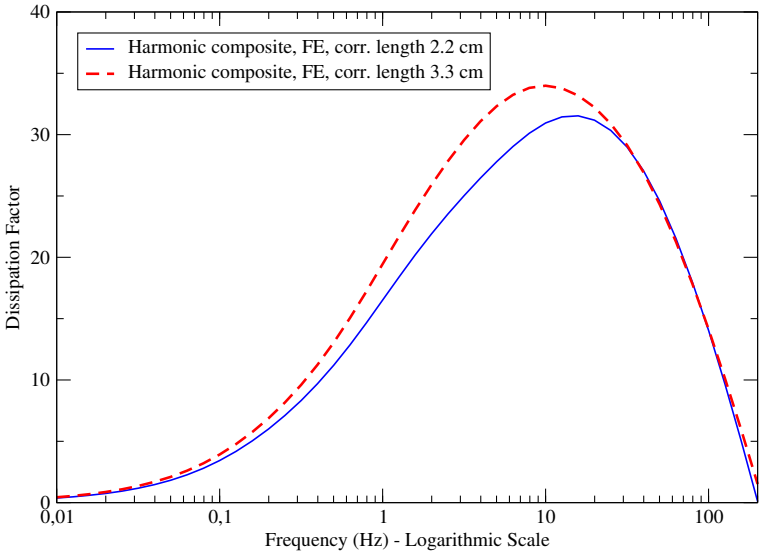


**Figure 11.** Effective P-wave dissipation coefficient as a function of frequency for the composite model and fractal binary ice content $I'$ as in Figures 6 (Correlation length is 3.33) and 7 (Correlation length is 2.22). The attenuation peak moves to higher frequencies for the shorter correlation length. Overall ice content is 36 %. The sample is a square of side length 10 cm.

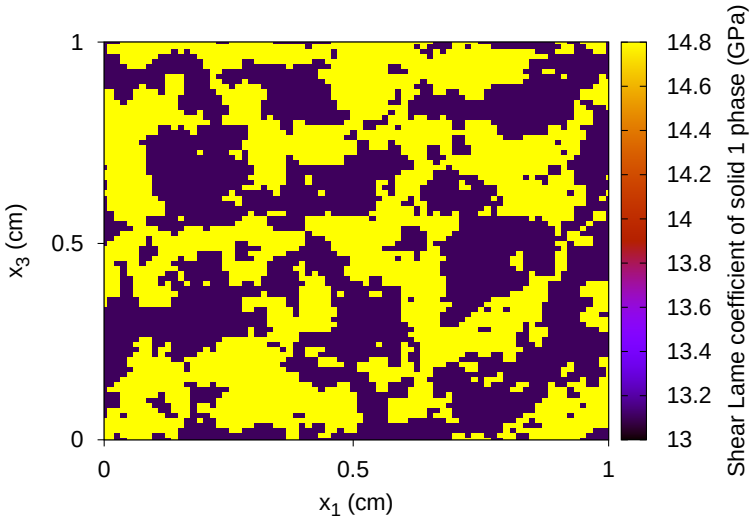


**Figure 12.** Lamé shear coefficient $\mu_1$ associated with a binary patchy ice content of correlation length is 0.04 cm and fractal dimension is $D = 2.2$. Overall ice content 41 %. The sample is a square of side length 1 cm.

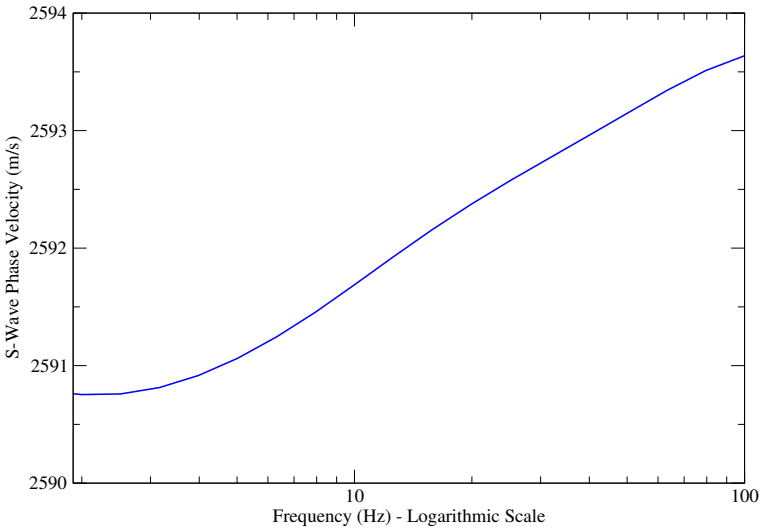


**Figure 13.** Effective S-wave phase velocity as function of frequency for the composite model and a binary patchy ice content of correlation length is 0.04 cm and overall ice content is 41 %. The sample is a square of side length 1 cm.